NANO LETTERS

pubs.acs.org/NanoLett

Letter

Phase-Changing in Graphite Assisted by Interface Charge Injection

Fei Pan, Kun Ni, Yue Ma, Hongjian Wu, Xiaoyu Tang, Juan Xiong, Yaping Yang, Chuanren Ye, Hong Yuan, Miao-Ling Lin, Jiayu Dai, Mengjian Zhu,* Ping-Heng Tan, Yanwu Zhu,* and Kostya S. Novoselov*

Cite This: *Nano Lett.* 2021, 21, 5648−5654

Read Online

ACCESS | Metrics & More | Article Recommendations | Supporting Information

ABSTRACT: Among many phase-changing materials, graphite is probably the most studied and interesting: the rhombohedral (3R) and hexagonal (2H) phases exhibit dramatically different electronic properties. However, up to now the only way to promote 3R to 2H phase transition is through exposure to elevated temperatures (above 1000 °C); thus, it is not feasible for modern technology. In this work, we demonstrate that 3R to 2H phase transition can be promoted by changing the charged state of 3D graphite, which promotes the repulsion between the layers and significantly reduces the energy barrier between the 3R and 2H phases. In particular, we show that charge transfer from lithium nitride (α-Li_3N) to graphite can lower the transition temperature down to 350 °C. The proposed interlayer slipping model potentially offers the control over topological states at the interfaces between different phases, making this system even more attractive for future electronic applications.

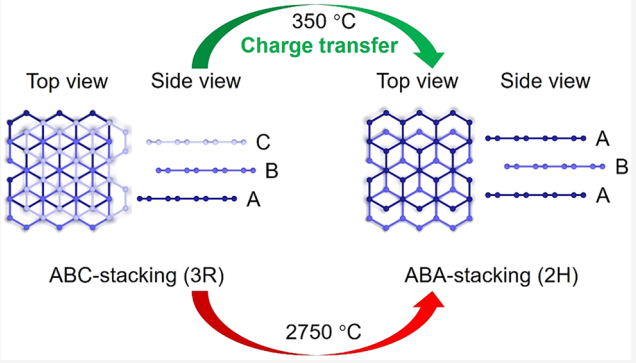

KEYWORDS: *graphite, rhombohedral phase, hexagonal phase, phase transition, interface charge injection*

Among many phase-changing materials,[1−4] the two-dimensional (2D) crystals hold a special place. The transitions are much easier to be obtained in 2D, since generally a lesser number of atoms is involved in domain wall movement. Thus, potentially it is possible to control the hysteresis associated with the transition and tune its parameters. Among the multiple 2D phase-changing materials,[5−9] few layer graphite is probably the most interesting one. Graphite can exist in two phases with remarkably different properties: the Bernal (2H, or ABA, Figure 1a) phase results in a semimetallic state where the overlap between the valence and the conduction bands depends on the number of layers,[10] and the rhombohedral (3R, or ABC, Figure 1a) phase has a gap opened in the bulk with topological states at the two surfaces.[11−15] Furthermore, the domain wall between the phases also has nontrivial electronic properties.[7,8]

Thus, it is very important to be able to control the transition between 2H and 3R phases. Unfortunately, the 3R phase, being metastable (the energy difference between ABA- and ABC-stackings has been calculated as 0.18 meV per atom)[10] can only be obtained by extraction from natural graphite (it accounts for ∼10% of naturally occurring graphite crystals)[16,17] or through micromechanical manipulations.[18] Furthermore, the 3R → 2H transition is usually observed at temperatures above 1000 °C, either through direct,[19] Joule,[20] or laser heating.[20] Clearly, such high temperatures make it completely inappropriate for modern electronic technologies.

In our work, we demonstrate that charging of 3R graphite (by exposing to lithium nitride) reduces the barrier between 3R and 2H phases (due to Coulombic repulsion) and brings the transition temperature to a comfortable 350 °C. Our conclusions are confirmed by the study of powder graphite samples (with transmission-mode *in-situ* X-ray diffraction (XRD)), micromechanically cleaved devices (with Raman spectroscopy), and density functional calculations.

We start with presenting our results on the bulk, powder graphite samples. Three batches (named #1, #2, and #3; details are shown in Table S1 in the Supporting Information) all with mixed phases of 2H and 3R were investigated. All three samples possess a flake morphology but with different lateral sizes (#1: 3−10 μm; #2: 1−4 μm; #3: 30−60 μm), as shown in scanning electron microscopy (SEM) images (Figure S1a,c,e in the Supporting Information). The XRD pattern of #1 graphite before annealing is shown in Figure 1b, consisting of the mixed diffraction features of 2H and 3R. Eleven peaks of the 2H phase and 10 peaks of the 3R phase are very consistent with

Received: March 26, 2021
Revised: June 20, 2021
Published: June 24, 2021

https://doi.org/10.1021/acs.nanolett.1c01225
Nano Lett. 2021, 21, 5648−5654

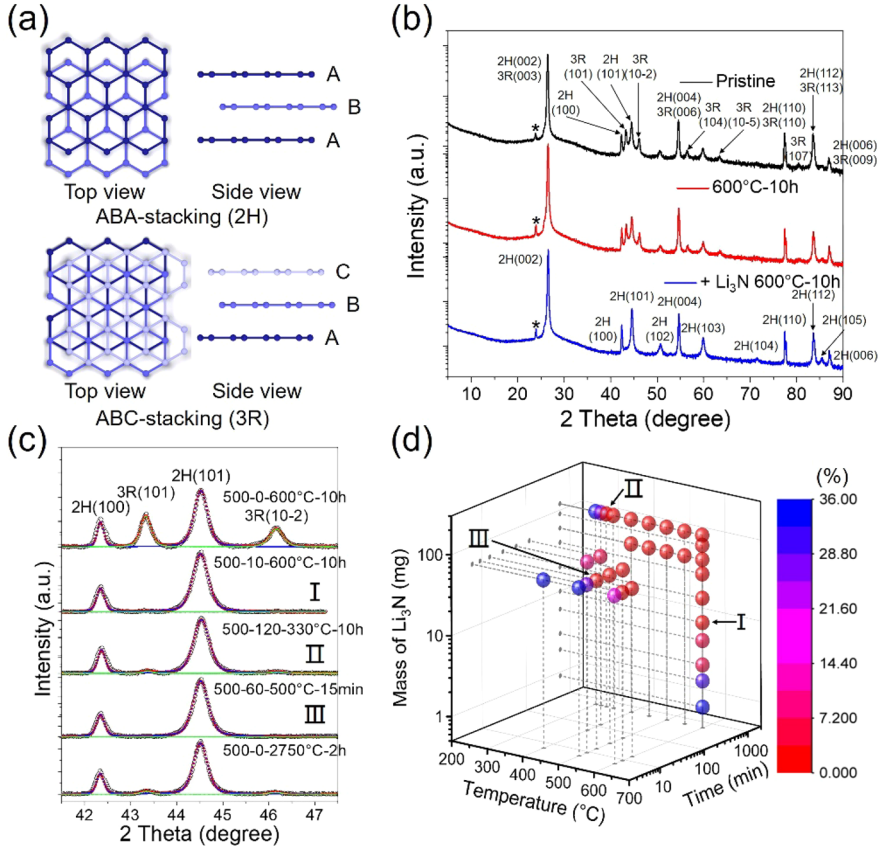

Figure 1. (a) Atomic models of ABA-stacking (2H phase) and ABC-stacking (3R phase) graphite. (b) Cu K_α (radiation wavelength λ = 0.15418 nm) powder XRD patterns of #1 graphite sample before annealing, after annealing at 600 °C for 10 h without or with α-Li_3N. Peaks corresponding to the 2H phase or 3R phase are indicated by the arrows, respectively. Asterisks (*) point to the diffraction peaks originated from Cu K_β (radiation wavelength λ = 0.13922 nm). (c) Fitting of Cu K_α (λ = 0.15418 nm) powder XRD patterns in the fingerprint range of 500 mg #1 graphite after annealing without α-Li_3N under 600 °C for 10 h; 500 mg #1 graphite after annealing with (I) 10 mg of α-Li_3N under 600 °C for 10 h, (II) 120 mg of α-Li_3N under 330 °C for 10 h, and (III) 60 mg of α-Li_3N under 500 °C for 15 min; 500 mg of #1 graphite after annealing without α-Li_3N under 2750 °C for 2 h. (d) Calculated 3R content (%) by fitting XRD data from #1 graphite after annealing with α-Li_3N (details are shown in Table S4 in the Supporting Information).

our simulation (Table S2 and Figure S2a,b). Five feature diffraction peaks (originated from crystal planes of (101), (10$\bar{2}$), (104), (10$\bar{5}$), (107) in the 3R phase, Figure 1b) are not overlapped with those of 2H phase and thus can be used to distinguish the crystal structure. Similar XRD patterns are observed for #2 graphite and #3 graphite (Figure S3a,b, Supporting Information). The XRD pattern of purchased Li_3N powder (Figure S4a, Supporting Information) shows that Li_3N is mainly composed of the α-phase with a small fraction of β-phase (see Figure S4b,c, Supporting Information, for the structure of α-phase and β-phase Li_3N).[21]

In a typical experiment, 500 mg of graphite powder and 120 mg of α-Li_3N powder were mixed in a quartz tube under Ar atmosphere, sealed in a vacuum, and then annealed at 600 °C in a tube furnace for 10 h (for details, please see Supporting Information). After annealing, all three graphite samples maintained the flake shape with sizes close to those of pristine samples, as shown in SEM images (Figure S1b,d,f in the Supporting Information). However, characteristic peaks of the 3R phase disappear in XRD, as seen in the blue lines of Figure 1b, Figure S3a,b (Supporting Information). At the same time, the intensities of diffraction peaks from the 2H phase (e.g., those corresponding to (101), (102), (103), (104), and (105) crystal planes) are enhanced in annealed samples, indicating the improved crystallinity of the 2H phase. Because of the highest proportion of the 3R phase among three types of graphite (3R content estimated from XRD patterns (Figure S5): #1: 37.657%; #2: 51.140%; #3: 26.380%), the most significant improvement of 2H peak intensity can be seen from #2 sample (blue line in Figure S3a).

Importantly, the samples annealed without α-Li_3N show completely different behaviors: as can be seen from the red lines of Figure 1b, and Figure S3a,b, the feature diffraction peaks of 3R phase remain unchanged, same as the black lines of Figure 1b and Figure S3a,b. At the same time, after annealing (either with or without the presence of α-Li_3N), we did not see any significant changes in the carbon-related features in Raman (Figure S6) or X-ray photoelectron spectroscopy (XPS, Figure S7); Also, no significant Li 1s and N 1s signals were detected in graphite annealed with α-Li_3N. The corresponding atomic ratio (Table S3) remains similar after annealing.

To obtain the 3R content after annealing, fitting of XRD patterns in the fingerprint range from 41.5° to 47.5° (covers 2H(100)/2H(101) and 3R(101)/3R(10$\bar{2}$) diffraction peaks)[22] was performed for all samples. Specifically, as shown in the detailed fitting in Figure 1c, for a 500 mg sample it only takes a small amount of α-Li_3N (less than 10 mg) to completely convert the 3R to 2H phase for the annealing performed at 600 °C for 10 h (Table S4 and Figure S8 for more data). When the

https://doi.org/10.1021/acs.nanolett.1c01225
Nano Lett. 2021, 21, 5648−5654

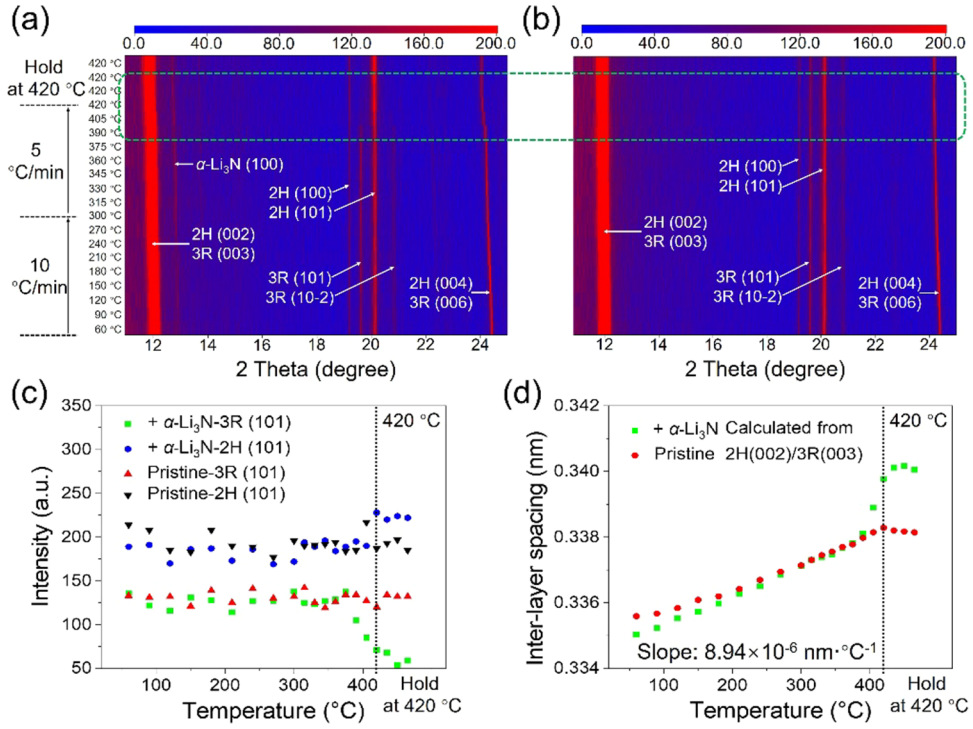

Figure 2. (a) Mo $K_{\alpha 1}$ (λ = 0.070926 nm) *in situ* XRD of #1 graphite sample annealing with α-Li_3N for a graphite/α-Li3N mass ratio of 200 mg/40 mg; (b) Mo $K_{\alpha 1}$ *in situ* XRD of #1 graphite sample annealing without α-Li_3N; (c) peak intensity evolutions of diffraction peaks for 3R(101) and 2H(101) versus temperature with or without α-Li_3N; (d) evolutions of interlayer spacing versus temperature with or without α-Li_3N.

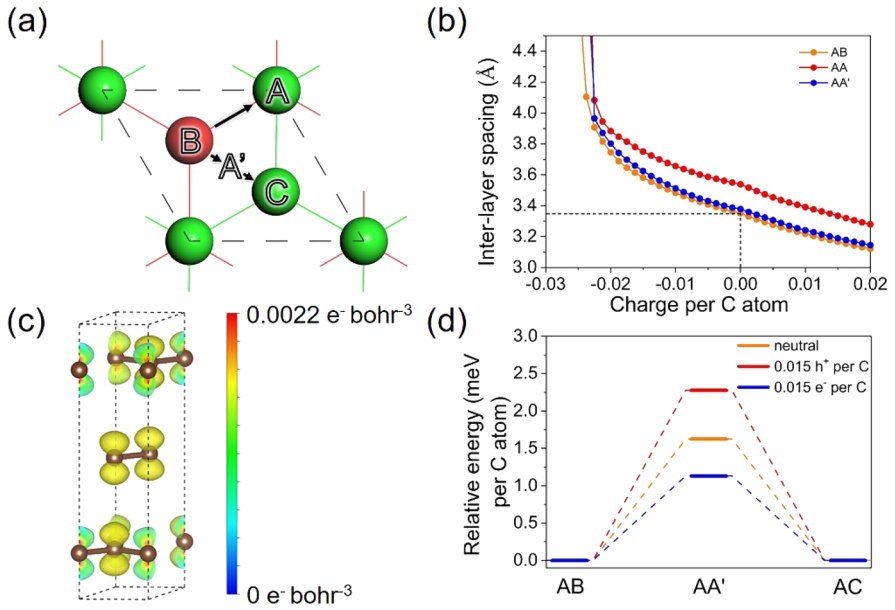

Figure 3. (a) Interlayer slipping pathway in 2H graphite. Layer A and Layer B in AB-stacking are drawn in green and red colors, respectively. If the red atom in Layer B is slipping along the different directions indicated by the arrows into marked positions like A, C, or A', the stacking would correspondingly become AA, AC, or AA', respectively; (b) evolution of interlayer spacing of AB, AA, and AA' graphite depending on the amount of injected charges. The dashed lines denote the inter spacing for the neutral situation; (c) charge differential density between negatively charged and neutral 3R graphite, where the isosurface value is 0.0005 e^- $bohr^{-3}$; (d) energy barrier for interlayer slipping of 2H graphite with or without charge injection.

mass of α-Li_3N is fixed as 120 mg and annealing duration as 10 h, an annealing at 330 °C reduced the 3R content to 3.225% and essentially maintains 0 for higher annealing temperatures (Table S4 and Figure S9). For annealing performed at 500 °C with 60 mg of α-Li_3N, the 3R content sharply decreases to 0 after 15 min annealing (Table S4 and Figure S10). Note that in the absence of α-Li_3N, there is still 4.987% 3R phase left even after 2 h of annealing at 2750 °C (Table S4 and Figure 1c). The change in the final mass of graphite after annealing is negligible (Figure S11). We have also found that alkali metals such as Li, Na, and K have a similar effect on the phase transition of 3R to 2H in #1 graphite, evidenced by XRD

https://doi.org/10.1021/acs.nanolett.1c01225
Nano Lett. 2021, 21, 5648−5654

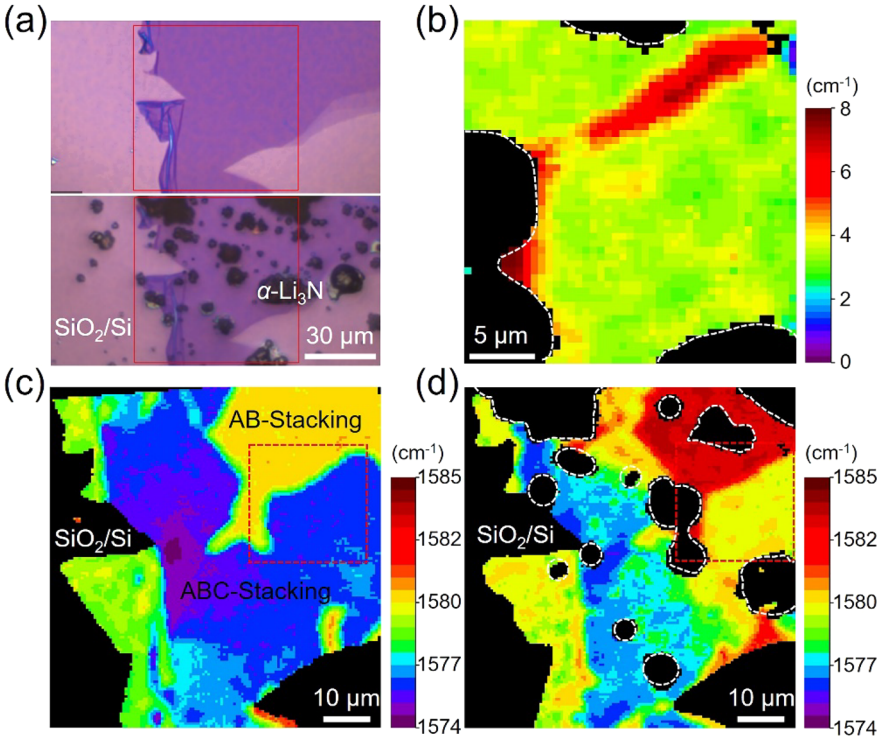

Figure 4. (a) Optical images of a mechanically exfoliated thin graphite flake on a SiO_2/Si substrate before (upper) and after (lower) partial coverage of α-Li_3N particles. (b) Mapping of the difference in the position of the Raman G band for the area marked by red dashed squares in (c) and (d); position mapping of the Raman G band excited by a 532 nm laser for the graphite flake on a SiO_2/Si substrate before (c) and after (d) partial coverage of α-Li_3N particles at the room temperature. The location of α-Li_3N particles in (b) and (d) is marked by white dashed lines.

studies (Figure S12). More experimental conditions for phase transition of the 3R phase are summarized in Figure 1d.

To further explore the phase transition process from 3R to 2H, transmission-mode *in-situ* XRD analysis (Mo $K_{\alpha 1}$, radiation wavelength λ = 0.070926 nm) was employed to track the stepwisely enhanced temperature response of #1 graphite. When the annealing temperature is increased from 60 to 420 °C, the real-time evolution of diffraction peaks corresponding to (002), (100), (101), (004) crystal planes of the 2H phase and (003), (101), (10$\bar{2}$), (006) crystal planes of 3R phase are recorded and shown in Figure 2a (with α-Li_3N) and Figure 2b (without α-Li_3N). From the comparison, we can see that all the peaks were consistent up to 390 °C, after which kinks in the position of the 2H(002)/3R(003) and 2H(004)/3R(006) peaks are observed for the case of annealing in the presence of α-Li_3N. Simultaneously, the intensity of (101) and (10$\bar{2}$) peaks of 3R phase gradually decays, as can be seen more clearly from Figure 2c, which compares the (101) peak intensities for 3R and 2H. The slight enhancement in the intensity of 2H(101) peak is consistent with the observation in Figure 1b. In contrast, for the case of annealing without α-Li_3N there is almost no change in the intensity of the (101) peak of the 3R phase and the (101) peak of the 2H phase. Calculated from 2H(002)/3R(003) diffraction peaks, the interlayer spacing of the graphite annealed with or without α-Li_3N is shown in Figure 2d. The observed gradient for the change of the lattice constant with temperature corresponds well to the reported thermal expansion rate of 9.054×10^{-6} nm·°C^{-1} for graphite along the *c*-axis.[23−26] Interestingly, the interlayer spacing of the graphite annealed with α-Li_3N jumps from 0.3381 to 0.3398 nm between 390 and 420 °C, while the interlayer spacing of the samples without α-Li_3N maintains the expansion rate up to 420 °C. After cooling down to room temperature, the interlayer spacing of the sample annealed with (without) α-Li_3N recovers to 0.3352 nm (0.3358 nm), close to the initial interlayer spacing of original #1 graphite measured at 60 °C.

It is clear that by annealing graphite in the presence of α-Li_3N we can achieve full conversion of 3R to 2H at temperatures between 350 and 400 °C, which is accompanied by an increase of the interlayer spacing. To investigate the role of α-Li_3N on the stacking transition of graphite, DFT simulations were carried out (see method in Supporting Information). The phase transition from 3R to 2H in graphite can be achieved via several sequential interlayer sliding pathways. As shown in Figure 3a, starting from AB-stacking, an AC-stacking in the bilayer could be obtained via two different routes. The first route is sliding of Layer B atoms to Position A and then to Position C, which has to overcome a barrier of 10.37 meV per atom (at AA-stacking configuration).[10] The second route is sliding of Layer B atoms to Position C via Position A', which has a much lower barrier of 1.62 meV at AA'-stacking, close to the reported value of 1.82 meV.[10] Thus, sliding of Layer B atoms to Position C via the intermediated state of AA' is the preferred route.

What is the mechanism of reduction of the energy barrier in the presence of α-Li_3N? On the basis of the experimental observations above, two scenarios are possible: intercalation of Li into the graphite[27,28] and charge transfer between α-Li_3N and graphite. From *in-situ* and *ex-situ* XRD, we did not see any sign of intercalation or of α-Li_3N structural change, and thus we can confirm that α-Li_3N neither decomposes nor reacts with graphite during the transition. At the same time, the layered structure of α-Li_3N is composed of hexagonal Li_2N and

https://doi.org/10.1021/acs.nanolett.1c01225
Nano Lett. 2021, 21, 5648−5654

Li^+ ion layers, enabling Li^+ ions to migrate perpendicular to the hexagonal *c*-axis with an exceptionally high conductivity of 1.2×10^{-3} S·cm^{-1} at 25 °C.[29] This makes possible formation of Li layer at the surface between graphite and α-Li_3N, thus allowing a significant charge transfer between these crystals.

The relationship between the interlayer spacing of AB, AA, or AA' stacked graphite and the amount of negative charge injection is shown in Figure 3b. We can see that the interlayer spacing is dramatically increased when more than 0.02 e^- per C atom is injected, corresponding to a Columbic explosion. Thus, 0.015 e^- per C atom has been adopted as a typical negative injection condition. On the basis of the charge differential density, as shown in Figure 3c, we find that the injected electrons occupy the p_z orbital of carbon atoms, leading to the stronger Columbic repulsion of π electrons between layers and enlarged interlayer distance. The sliding barriers are also calculated by the solid state nudged elastic band (SSNEB) method,[30] as shown in Figure 3d. We can see that the sliding barrier decreases from 1.625 to 1.131 meV upon electron injection, while it increases to 2.278 meV with hole injection. Different calculation methods compared in Table S5 give consistent results. In addition, Bader analysis shown in Figure S16 indicates 0.076 e^- per carbon atom transferred from the 001-Li face of α-Li_3N into graphene. We can see that the negative charge injection (electron doping) would enlarge the interlayer spacing, and thus, the van der Waals interaction between layers is weakened. Therefore, the interface charge injection from α-Li_3N to graphite crystals may have led to the interlayer-decoupling effect.[31] The reduced interlayer interaction would make the layer slipping occur more easily, causing a lower phase transition temperature from 3R to 2H in graphite.

To further confirm the doping caused by α-Li_3N, Raman mapping is performed at the room temperature on mechanically exfoliated graphite flakes transferred onto a SiO_2/Si substrate, before and after the partial coverage of α-Li_3N particles (please see Supporting Information for experimental details), as shown in Figure 4a. The difference of the Raman G band position in the same area has been mapped (Figure 4b), based on the G band position mapping on the area before (Figure 4c) and after (Figure 4d) introduction of α-Li_3N particles. From Figure 4c, the AB-stacking and ABC-stacking regions can be clearly identified by the G band position.[32] Precise calibration of the mappings in Figure 4c,d was carried out by considering the distortion and location errors in the scanning. The calculated G band position difference (subtracting Figure 4c from Figure 4d) is shown in Figure S13a, from which we can see that the presence of α-Li_3N generally induces a blue shift of the G band. A close comparison in Figure 4b, by taking the region marked by the red dashed squares (containing 50 × 50 points) in Figure 4, panel c or d, confirms a blue shift of the G band without showing any obvious dependence on the distance from α-Li_3N particles in the range of interest. Another comparison based on a thin graphite flake (Figure S14), which is characterized as almost all AB-stacking, has confirmed the same effect of α-Li_3N on the Raman G band position (Figure S13b). The G band blueshift caused by α-Li_3N is robust, independent of the original stacking in the graphite, but an exceptionally large difference along the AB/ABC domain walls is observed in Figure 4b.

Previous studies have indicated that the blue shift of the G band can be related to the slight or moderate electron/hole doping into the thin graphite films.[33−36] Moreover, it has been determined that the free-energy difference between the two stacking configurations scales quadratically with the electric field, and thus ABC-stacking is favored as the electric field increases.[7] Therefore, combing all the experimental evidence and simulations, we argue that the electron doping caused by α-Li_3N, which could induce an exceptionally strong electric field at the domain walls between 2H and 3R phases, would drive the phase transition in a much lower temperature range with the help of a globally larger interlayer distance. In fact, we have observed an obvious change of the G and 2D band when a graphite flake covered with α-Li_3N was subjected to annealing in an *in-situ* Raman spectroscopy (Figure S15), which could further support the electron transfer[31] and the triggering of phase transition.[37,38]

In summary, a stacking order phase transition of 3R to 2H in graphite has been achieved by annealing the graphite with α-Li_3N below 400 °C. With analysis of the structural evolution depending on the amount of α-Li_3N and temperature, the phase transition mechanism has been emphasized by an interface charge injection from α-Li_3N to the conjugated π bond of graphite. The decoupling between layers in the presence of α-Li_3N has been evidenced by the obvious expansion of the interlayer distance with *in situ* X-ray diffraction. Our simulation further proposed an interlayer slipping pathway of AB to AC via AA' to explain the stacking order phase transition, which demonstrates a lower sliding barrier and expanded interlayer distance upon negative charging.

■ ASSOCIATED CONTENT

Supporting Information

The Supporting Information is available free of charge at https://pubs.acs.org/doi/10.1021/acs.nanolett.1c01225.

Additional details regarding the experiments, characterizations, and simulation methods along with additional measurements and DFT calculations supporting our conclusions (PDF)

■ AUTHOR INFORMATION

Corresponding Authors

Mengjian Zhu − *College of Advanced Interdisciplinary Studies, National University of Defense Technology, Changsha, Hunan 410073, P. R. China;* orcid.org/0000-0002-7863-2660; Email: zhumengjian11@nudt.edu.cn

Yanwu Zhu − *Hefei National Research Center for Physical Sciences at the Microscale, & CAS Key Laboratory of Materials for Energy Conversion & Department of Materials Science and Engineering, University of Science and Technology of China, Hefei, Anhui 230026, P. R. China;* orcid.org/0000-0002-7505-1502; Email: zhuyanwu@ustc.edu.cn

Kostya S. Novoselov − *National Graphene Institute, University of Manchester, Manchester M13 9PL, United Kingdom; Centre for Advanced 2D Materials, National University of Singapore, 117546, Singapore; Chongqing 2D Materials Institute, Chongqing 400714, P. R. China;* Email: kostya@nus.edu.sg

Authors

Fei Pan − *Hefei National Research Center for Physical Sciences at the Microscale, & CAS Key Laboratory of Materials for*

https://doi.org/10.1021/acs.nanolett.1c01225
Nano Lett. 2021, 21, 5648−5654

Energy Conversion & Department of Materials Science and Engineering, University of Science and Technology of China, Hefei, Anhui 230026, P. R. China

Kun Ni − *Hefei National Research Center for Physical Sciences at the Microscale, & CAS Key Laboratory of Materials for Energy Conversion & Department of Materials Science and Engineering, University of Science and Technology of China, Hefei, Anhui 230026, P. R. China*

Yue Ma − *State Key Laboratory of Solidification Processing, & Center for Nano Energy Materials, & School of Materials Science and Engineering, Northwestern Polytechnical University & Shaanxi Joint Laboratory of Graphene (NPU), Xi' an, Shaanxi 710072, P. R. China;* orcid.org/0000-0002-1005-9386

Hongjian Wu − *Department of Physics, National University of Defense Technology, Changsha, Hunan 410073, P. R. China*

Xiaoyu Tang − *State Key Laboratory of Solidification Processing, & Center for Nano Energy Materials, & School of Materials Science and Engineering, Northwestern Polytechnical University & Shaanxi Joint Laboratory of Graphene (NPU), Xi' an, Shaanxi 710072, P. R. China*

Juan Xiong − *Hefei National Research Center for Physical Sciences at the Microscale, & CAS Key Laboratory of Materials for Energy Conversion & Department of Materials Science and Engineering, University of Science and Technology of China, Hefei, Anhui 230026, P. R. China*

Yaping Yang − *Science and Technology on Advanced Ceramic Fibers and Composites Laboratory, College of Aerospace Science and Engineering, National University of Defense Technology, Changsha, Hunan 410073, P. R. China*

Chuanren Ye − *Hefei National Research Center for Physical Sciences at the Microscale, & CAS Key Laboratory of Materials for Energy Conversion & Department of Materials Science and Engineering, University of Science and Technology of China, Hefei, Anhui 230026, P. R. China*

Hong Yuan − *Hefei National Research Center for Physical Sciences at the Microscale, & CAS Key Laboratory of Materials for Energy Conversion & Department of Materials Science and Engineering, University of Science and Technology of China, Hefei, Anhui 230026, P. R. China*

Miao-Ling Lin − *State Key Laboratory of Superlattices and Microstructures, Institute of Semiconductors, Chinese Academy of Sciences, Beijing 100083, P. R. China*

Jiayu Dai − *Department of Physics, National University of Defense Technology, Changsha, Hunan 410073, P. R. China;* orcid.org/0000-0001-7423-7500

Ping-Heng Tan − *State Key Laboratory of Superlattices and Microstructures, Institute of Semiconductors, Chinese Academy of Sciences, Beijing 100083, P. R. China;* orcid.org/0000-0001-6575-1516

Complete contact information is available at: https://pubs.acs.org/10.1021/acs.nanolett.1c01225

Author Contributions

●F.P., K.N. and Y.M. contributed equally to this work. F.P. and Y.Z. conceived the experiments. F.P. conducted the preparation experiments, analyzed the data, and drafted the manuscript. K.N. performed the fitting of Cu K_α (radiation wavelength λ = 0.15418 nm) powder XRD data, analysis of Raman mapping data, and DFT calculations. X.T. and Y.M. performed the characterization of *in situ* XRD. H.W., Y.Y., J.X., M.Z., and J.D. performed the preparation of FLG flakes and Raman mapping of FLG flakes before and after introduction of α-Li_3N particles. H.Y. performed the graphitization of #1 graphite powder under 2750 °C. C.Y. performed the SEM characterizations of #1, #2, and #3 graphite powder before and after annealing with α-Li_3N. M.Z. and P.-H.T. helped to analyze the Raman data. Y.Z. and K.S.N. supervised the study and revised the manuscript. All authors discussed the results and commented on the manuscript.

Notes

The authors declare no competing financial interest.

■ ACKNOWLEDGMENTS

This work was supported by National Key R&D Program of China (Grant Nos. 2020YFA0711502, 2018YFA0306900) and Natural Science Foundation of China (Nos. 51772282, 51972299, 52003265, 51711530037, 11804386). K.S.N. also acknowledges support from EU Flagship Programs (Graphene CNECTICT-604391 and 2D-SIPC Quantum Technology), European Research Council Synergy Grant Hetero2D, the Royal Society, and EPSRC grants EP/N010345/1, EP/P026850/1, EP/S030719/1.

■ REFERENCES

(1) Wuttig, M.; Yamada, N. Phase-change materials for rewriteable data storage. *Nat. Mater.* **2007**, *6* (11), 824−832.

(2) Lencer, D.; Salinga, M.; Grabowski, B.; Hickel, T.; Neugebauer, J.; Wuttig, M. A map for phase-change materials. *Nat. Mater.* **2008**, *7* (12), 972−977.

(3) Jager, M. F.; Ott, C.; Kraus, P. M.; Kaplan, C. J.; Pouse, W.; Marvel, R. E.; Haglund, R. F.; Neumark, D. M.; Leone, S. R. Tracking the insulator-to-metal phase transition in VO_2 with few-femtosecond extreme UV transient absorption spectroscopy. *Proc. Natl. Acad. Sci. U. S. A.* **2017**, *114* (36), 9558−9563.

(4) Yang, H.; Kim, S. W.; Chhowalla, M.; Lee, Y. H. Structural and quantum-state phase transitions in van der Waals layered materials. *Nat. Phys.* **2017**, *13* (10), 931−937.

(5) Lin, Y.-C.; Dumcenco, D. O.; Huang, Y.-S.; Suenaga, K. Atomic mechanism of the semiconducting-to-metallic phase transition in single-layered MoS_2. *Nat. Nanotechnol.* **2014**, *9* (5), 391−396.

(6) Wang, Y.; Xiao, J.; Zhu, H.; Li, Y.; Alsaid, Y.; Fong, K. Y.; Zhou, Y.; Wang, S.; Shi, W.; Wang, Y.; Zettl, A.; Reed, E. J.; Zhang, X. Structural phase transition in monolayer $MoTe_2$ driven by electrostatic doping. *Nature* **2017**, *550* (7677), 487−491.

(7) Yankowitz, M.; Wang, J. I-J.; Birdwell, A. G.; Chen, Y.-A.; Watanabe, K.; Taniguchi, T.; Jacquod, P.; San-Jose, P.; Jarillo-Herrero, P.; LeRoy, B. J. Electric field control of soliton motion and stacking in trilayer graphene. *Nat. Mater.* **2014**, *13* (8), 786−789.

(8) Jiang, L.; Wang, S.; Shi, Z.; Jin, C.; Utama, M. I. B.; Zhao, S.; Shen, Y.-R.; Gao, H.-J.; Zhang, G.; Wang, F. Manipulation of domain-wall solitons in bi-and trilayer graphene. *Nat. Nanotechnol.* **2018**, *13* (3), 204−208.

(9) Li, H.; Utama, M. I. B.; Wang, S.; Zhao, W.; Zhao, S.; Xiao, X.; Jiang, Y.; Jiang, L.; Taniguchi, T.; Watanabe, K.; Weber-Bargioni, A.; Zettl, A.; Wang, F. Global Control of Stacking-Order Phase Transition by Doping and Electric Field in Few-Layer Graphene. *Nano Lett.* **2020**, *20* (5), 3106−3112.

(10) Aoki, M.; Amawashi, H. Dependence of band structures on stacking and field in layered graphene. *Solid State Commun.* **2007**, *142* (3), 123−127.

(11) Kopnin, N.; Ijäs, M.; Harju, A.; Heikkilä, T. High-temperature surface superconductivity in rhombohedral graphite. *Phys. Rev. B: Condens. Matter Mater. Phys.* **2013**, *87* (14), 140503.

(12) Pierucci, D.; Sediri, H.; Hajlaoui, M.; Girard, J.-C.; Brumme, T.; Calandra, M.; Velez-Fort, E.; Patriarche, G.; Silly, M. G.; Ferro, G.; Souliere, V.; Marangolo, M.; Sirotti, F.; Mauri, F.; Ouerghi, A. Evidence for Flat Bands near the Fermi Level in Epitaxial

Rhombohedral Multilayer Graphene. *ACS Nano* **2015**, *9* (5), 5432−5439.
(13) Ho, C.-H.; Chang, C.-P.; Lin, M.-F. Evolution and dimensional crossover from the bulk subbands in ABC-stacked graphene to a three-dimensional Dirac cone structure in rhombohedral graphite. *Phys. Rev. B: Condens. Matter Mater. Phys.* **2016**, *93* (7), 075437.
(14) Pamuk, B.; Baima, J.; Mauri, F.; Calandra, M. Magnetic gap opening in rhombohedral-stacked multilayer graphene from first principles. *Phys. Rev. B: Condens. Matter Mater. Phys.* **2017**, *95* (7), 075422.
(15) Shi, Y.; Xu, S.; Yang, Y.; Slizovskiy, S.; Morozov, S. V.; Son, S.-K.; Ozdemir, S.; Mullan, C.; Barrier, J.; Yin, J.; Berdyugin, A. I.; Piot, B. A.; Taniguchi, T.; Watanabe, K.; Fal'ko, V. I.; Novoselov, K. S.; Geim, A. K.; Mishchenko, A. Electronic phase separation in multilayer rhombohedral graphite. *Nature* **2020**, *584* (7820), 210−214.
(16) Fahy, S.; Louie, S. G.; Cohen, M. L. Pseudopotential total-energy study of the transition from rhombohedral graphite to diamond. *Phys. Rev. B: Condens. Matter Mater. Phys.* **1986**, *34* (2), 1191.
(17) Bacon, G. A note on the rhombohedral modification of graphite. *Acta Crystallogr.* **1950**, *3* (4), 320−320.
(18) Yang, Y.; Zou, Y.-C.; Woods, C. R.; Shi, Y.; Yin, J.; Xu, S.; Ozdemir, S.; Taniguchi, T.; Watanabe, K.; Geim, A. K.; Novoselov, K. S.; Haigh, S. J.; Mishchenko, A. Stacking Order in Graphite Films Controlled by van der Waals Technology. *Nano Lett.* **2019**, *19* (12), 8526−8532.
(19) Matuyama, E. Rate of transformation of rhombohedral graphite at high temperatures. *Nature* **1956**, *178* (4548), 1459−1460.
(20) Latychevskaia, T.; Son, S.-K.; Yang, Y.; Chancellor, D.; Brown, M.; Ozdemir, S.; Madan, I.; Berruto, G.; Carbone, F.; Mishchenko, A.; Novoselov, K. S. Stacking transition in rhombohedral graphite. *Front. Phys.* **2019**, *14* (1), 13608.
(21) Li, W.; Wu, G.; Araújo, C. M.; Scheicher, R. H.; Blomqvist, A.; Ahuja, R.; Xiong, Z.; Feng, Y.; Chen, P. Li^+ ion conductivity and diffusion mechanism in α-Li_3N and β-Li_3N. *Energy Environ. Sci.* **2010**, *3* (10), 1524−1530.
(22) Guerin, K.; Fevrierbouvier, A.; Flandrois, S.; Couzi, M.; Simon, B.; Biensan, P. Effect of Graphite Crystal Structure on Lithium Electrochemical Intercalation. *J. Electrochem. Soc.* **1999**, *146* (10), 3660−3665.
(23) Nelson, J.; Riley, D. The thermal expansion of graphite from 15 °C. to 800 °C.: part I. Experimental. *Proc. Phys. Soc.* **1945**, *57* (6), 477.
(24) Riley, D. The thermal expansion of graphite: part II. Theoretical. *Proc. Phys. Soc.* **1945**, *57* (6), 486.
(25) Steward, E.; Cook, B. X-ray measurement of thermal expansion perpendicular to the layer planes of artificial and natural graphites. *Nature* **1960**, *185* (4706), 78−80.
(26) Tsang, D.; Marsden, B.; Fok, S.; Hall, G. Graphite thermal expansion relationship for different temperature ranges. *Carbon* **2005**, *43* (14), 2902−2906.
(27) Guerard, D.; Herold, A. Intercalation of lithium into graphite and other carbons. *Carbon* **1975**, *13* (4), 337−345.
(28) Basu, S.; Zeller, C.; Flanders, P.; Fuerst, C.; Johnson, W.; Fischer, J. Synthesis and properties of lithium-graphite intercalation compounds. *Mater. Sci. Eng.* **1979**, *38* (3), 275−283.
(29) Alpen, U. V.; Rabenau, A.; Talat, G. Ionic conductivity in Li_3N single crystals. *Appl. Phys. Lett.* **1977**, *30* (12), 621−623.
(30) Sheppard, D.; Xiao, P.; Chemelewski, W.; Johnson, D. D.; Henkelman, G. A generalized solid-state nudged elastic band method. *J. Chem. Phys.* **2012**, *136* (7), 074103.
(31) Kim, S.; Park, J.; Duong, D. L.; Cho, S.; Kim, S. W.; Yang, H. Proximity Engineering of the van der Waals Interaction in Multilayered Graphene. *ACS Appl. Mater. Interfaces* **2019**, *11* (45), 42528−42533.
(32) Zhang, J.; Han, J.; Peng, G.; Yang, X.; Yuan, X.; Li, Y.; Chen, J.; Xu, W.; Liu, K.; Zhu, Z.; Cao, W.; Han, Z.; Dai, J.; Zhu, M.; Qin, S.; Novoselov, K. S. Light-induced irreversible structural phase transition in trilayer graphene. *Light: Sci. Appl.* **2020**, *9* (1), 174.
(33) Das, A.; Pisana, S.; Chakraborty, B.; Piscanec, S.; Saha, S. K.; Waghmare, U. V.; Novoselov, K. S.; Krishnamurthy, H. R.; Geim, A. K.; Ferrari, A. C.; Sood, A. K. Monitoring dopants by Raman scattering in an electrochemically top-gated graphene transistor. *Nat. Nanotechnol.* **2008**, *3* (4), 210−215.
(34) Jung, N.; Kim, N.; Jockusch, S.; Turro, N. J.; Kim, P.; Brus, L. Charge Transfer Chemical Doping of Few Layer Graphenes: Charge Distribution and Band Gap Formation. *Nano Lett.* **2009**, *9* (12), 4133−4137.
(35) Kalbac, M.; Reina-Cecco, A.; Farhat, H.; Kong, J.; Kavan, L.; Dresselhaus, M. S. The Influence of Strong Electron and Hole doping on the Raman Intensity of Chemical Vapor-Deposition Graphene. *ACS Nano* **2010**, *4* (10), 6055−6063.
(36) Wu, J.-B.; Lin, M.-L.; Cong, X.; Liu, H.-N.; Tan, P.-H. Raman spectroscopy of graphene-based materials and its applications in related devices. *Chem. Soc. Rev.* **2018**, *47* (5), 1822−1873.
(37) Kim, S.; Song, S.; Park, J.; Yu, H. S.; Cho, S.; Kim, D.; Baik, J.; Choe, D.-H.; Chang, K. J.; Lee, Y. H.; Kim, S. W.; Yang, H. Long-Range Lattice Engineering of $MoTe_2$ by a 2D Electride. *Nano Lett.* **2017**, *17* (6), 3363−3368.
(38) Dhakal, K. P.; Ghimire, G.; Chung, K.; Duong, D. L.; Kim, S. W.; Kim, J. Probing Multiphased Transition in Bulk MoS_2 by Direct Electron Injection. *ACS Nano* **2019**, *13* (12), 14437−14446.

https://doi.org/10.1021/acs.nanolett.1c01225
Nano Lett. 2021, 21, 5648−5654

Supporting Information for

"Phase-Changing in Graphite Assisted by Interface Charge Injection"

Fei Pan,[1,‡] Kun Ni,[1,‡] Yue Ma,[2,‡] Hongjian Wu,[3] Xiaoyu Tang,[2] Juan Xiong,[1] Yaping Yang,[4] Chuanren Ye,[1] Hong Yuan,[1] Miao-Ling Lin,[6] Jiayu Dai,[3] Mengjian Zhu,[5,*] Ping-Heng Tan,[6] Yanwu Zhu[1,*], Kostya S. Novoselov[7,*]

[1] Hefei National Research Center for Physical Sciences at the Microscale, &
CAS Key Laboratory of Materials for Energy Conversion, &
Department of Materials Science and Engineering,
University of Science and Technology of China,
96 Jin Zhai Rd., Hefei, Anhui 230026, P. R. China
[2] State Key Laboratory of Solidification Processing, &
Center for Nano Energy Materials, &
School of Materials Science and Engineering,
Northwestern Polytechnical University, &
Shaanxi Joint Laboratory of Graphene (NPU), Xi' an, Shaanxi 710072, P.R. China
[3] Department of Physics,
National University of Defense Technology, Changsha, Hunan 410073, P. R. China
[4] Science and Technology on Advanced Ceramic Fibers and Composites Laboratory,
College of Aerospace Science and Engineering,
National University of Defense Technology, Changsha, Hunan 410073, P. R. China
[5] College of Advanced Interdisciplinary Studies,
National University of Defense Technology, Changsha, Hunan 410073, P. R. China
[6] State Key Laboratory of Superlattices and Microstructures,
Institute of Semiconductors,
Chinese Academy of Sciences, Beijing 100083, P. R. China
[7] National Graphene Institute, University of Manchester,
Oxford Road, Manchester, M13 9PL, United Kingdom, &
Centre for Advanced 2D Materials, National University of Singapore, 117546, Singapore, & Chongqing 2D Materials Institute, Liangjiang New Area, Chongqing 400714, P. R. China

‡ These authors equally contributed to this work.

* Corresponding Authors.

E-mails: zhumengjian11@nudt.edu.cn; zhuyanwu@ustc.edu.cn; kostya@nus.edu.sg

Experimental Section

Experiments: The graphite flakes with graininess of 8000 mesh (99.95%, metals basis, named as #1) and of 600 nm (D50 < 600 nm, 99.95%, metals basis, named as #2) were purchased from Aladdin Industrial Corporation (Shanghai, China). The graphite flake with graininess of ≤ 30 μm (≥ 95%, C content ≥ 99.85%, named as #3) were purchased from Sinopharm Chemical Reagent Co., Ltd (Shanghai, China) and details listed in Table S1. Lithium nitride (α-Li_3N, ≥99.5%, metals basis) powder with graininess of ~ 80 mesh was purchased from Sigma-Aldrich. Lithium nitride (α-Li_3N, ≥ 99.4%, metals basis) powder with graininess of ~ 60 mesh was purchased from Alfa Aesar. In a typical experiment, 500 mg graphite powder was loaded into a quartz tube (length: 150 mm; diameter: 15 mm) and 120 mg α-Li_3N powder was added in the same tube in a glove box under Ar atmosphere. One shall note that 1000 mg #1 graphite samples were used for the mass ratios of 500-6, 500-3, 500-1.9 and 500-0.9 (corresponding to experiments of 1000 mg - 12 mg, 1000 mg - 6 mg, 1000 mg - 3.8 mg and 1000 mg - 1.8 mg) to ensure the weighing accuracy of α-Li_3N powders in the Ar glove box. Then two powders were mixed by shaking the tube and then sealed in vacuum. The sealed quartz tube with samples was heated to 600 °C with a heating rate of 5 °C·min^{-1} in Ar atmosphere (flowing rate of 100 sccm) in a horizontal tube furnace, followed by annealing for 10 h. In the experiments with alkali metals like Li, Na and K, α-Li_3N powder was replaced by Li, Na and K foils, and added in the quartz tube in a glove box under Ar atmosphere. After annealing, the samples were washed by deionized water and ethanol successively and then dried at 60 °C in ambience. In the Raman mapping analysis, few-layer graphite (FLG) flakes were obtained by mechanical exfoliation from bulk graphite crystals (flaggy graphite, purchased from NGS, Germany) onto a substrate with a 285 nm SiO_2 capping layer on top of heavily doped silicon.

Characterizations: Scanning electron microscopy (SEM) images were obtained by a field-emission scanning electron microscope (FEI, Apreo, operating at 2 kV, US). Annealing of #1 graphite powder under 2750 °C was performed by a graphitization furnace (Series LF Top Loading Multi-Purpose Furnace, Centorr Vacuum Industries, USA). X-ray diffraction (XRD) patterns were measured via a high-resolution X-ray diffractometer (Cu K_α radiation with wavelength of 0.15418 nm, operating at 40 kV and 30 mA, Rigaku SmartLab 3kW, Japan) with a scan rate of 10 ° • min^{-1}. Data were collected in the range from 5 ° to 90 ° at a 0.02 ° resolution. The X-ray photoelectron spectra (XPS) were performed on an XPS facility with Al K_α radiation (hν = 1486.6 eV) (Thermo Scientific, ESCALAB 250, US). *In-situ* X-ray diffraction (*In-situ* XRD) analysis were performed in a transmission-mode X-ray diffractometer (STADIP STOE, Germany) with a position-sensitive detector and Mo $K_{\alpha1}$ radiation with wavelength of 0.070926 nm, operating at 50 kV and 40 mA. 200 mg #1 graphite sample with 40 mg or without α-Li_3N powder were sealed into glass Lindemann capillaries (length: 80 mm, outer diameter: 0.5 mm, wall thickness: 0.01 mm; Hilgenberg, Germany) for *In-situ* XRD analysis in glove box under Ar atmosphere. Before mixing, the #1 graphite sample was dried in vacuum at 200 °C for 12 h to remove any absorbed water. A N_2 flow with rate of ~ 1 L • min^{-1} was applied on the glass Lindemann capillaries during the sealing with silicon grease, to ensure that α-Li_3N powder will not be contaminated by water and

oxygen in the air. The Raman spectra of graphite powder were measured with a Raman spectroscopy (Renishaw inVia Raman Micro-scope, 532 nm, UK). Raman spectroscopy of FLG flakes was performed with a confocal Raman spectrometer (Witec Alpha 300R, Germany). The laser wavelength was 532 nm, and the diameter of the laser spot was ~ 0.6 μm. The spectral resolution of the Raman spectra was about 1 cm^{-1} using a grating of 600 grooves per mm. The Raman spectra were calibrated by 520.4 cm^{-1} peak of the silicon substrate. To compare the Raman results before and after introduction of α-Li_3N, as-exfoliated intrinsic FLG flakes were sealed in a transparent quartz cell and first time characterized by Raman mapping. The laser power was 5 mW and the integration time was 0.05 s per pixel. After first Raman scanning, α-Li_3N particles were transferred onto the FLG flakes using a van der Waals dry transfer setup in a glove box with Ar atmosphere. To avoid additional doping, the transfer process of α-Li_3N particles onto FLG flakes does not involve any polymer and solvent. First, the FLG flakes were exfoliated onto a silicon wafer and the α-Li_3N particles were deposited on a transparent glass slide. The glass slide was then flipped and some particles can be adsorbed on the slide due to van der Waals force. Then we used a home-built dry transfer facility in a glove box to translate the flipped glass slide above the graphene/silicon and aligned the α-Li_3N particles with the marked FLG samples by an optical microscope and a mechanical manipulator. After that, we gently pressed the glass slide on top of the FLG. Some particles can be transferred to the FLG samples in this way. The α-Li_3N covered FLG flakes were sealed in the same quartz cell for the second time Raman scanning. The Raman mapping data with α-Li_3N was stretched and rotated to make sure it can be precisely aligned with the Raman mapping data without α-Li_3N at pixel level. The *in-situ* Raman was performed with a Raman spectroscopy (LabRAM HR Evolution, HORIBA Scientific, France) by placing the α-Li_3N covered FLG flakes in a heating component (LinKam THMSG600).

Simulation methods: All the DFT simulations were done by Vienna Ab-initio Simulation Package (VASP) software.[1] The energy cutoff for plane wave basis set is 500 eV. All calculations were done with spin unrestricted under generalized gradient approximation (GGA).[2] The energy tolerance for self-consistent field (SCF) iteration was 1×10^{-8} eV. The force tolerance for geometry optimization was 1×10^{-4} eV/Å. Gaussian type smearing was used with sigma value of 0.05 eV. The exchange correlation function was chosen as optB88-vdW[3] after careful tests and comparisons with PBE-BJD3 [4,5] and newly developed SCAN-rvv10 [6] function, as shown in Table S5. The charge injection was achieved by setting NELECT parameter as the total number of calculated valance electrons. The quantitative phase analysis (QPA) of XRD data was done by using Reflex code embedded in Materials Studio software. The phase of ideal 2H and 3R graphite was obtained from DFT calculations with optB88-vdW functional. To get a more reliable and repeatable result, the background line of experimental XRD data was removed by JADE software and the XRD data is horizontally moved to make the 2H (101) peak have a good alignment with the calculated peak from the ideal 2H phase. Minor deviations between experiment and simulation shall be related to the fact that the Cu K_α radiation (λ = 0.15418 nm) used in powder XRD consists of Cu $K_{\alpha1}$ (λ = 0.15405 nm) and Cu $K_{\alpha2}$ (λ = 0.15443 nm), among which the intensity of the former is about twice as the latter (100:49.7).[7] Note that the horizontal movement of the peaks do not have any influence on the intensity of the peak, thus should not introduce extra errors for QPA fitting. The X-ray wavelength is 0.15418

nm with the copper source. Lattice parameters are optimized with fractional coordinates of the atoms fixed during refinement for samples. Pesudo-Voigt[8] function is used to fit peak shapes. Crystallite size of A and B is optimized while C is fixed as 500 Å. The lattice strain of C is optimized while A and B is fixed as 0.01%. The background fitting in Reflex code is turned off because the background has already been removed in JADE software.

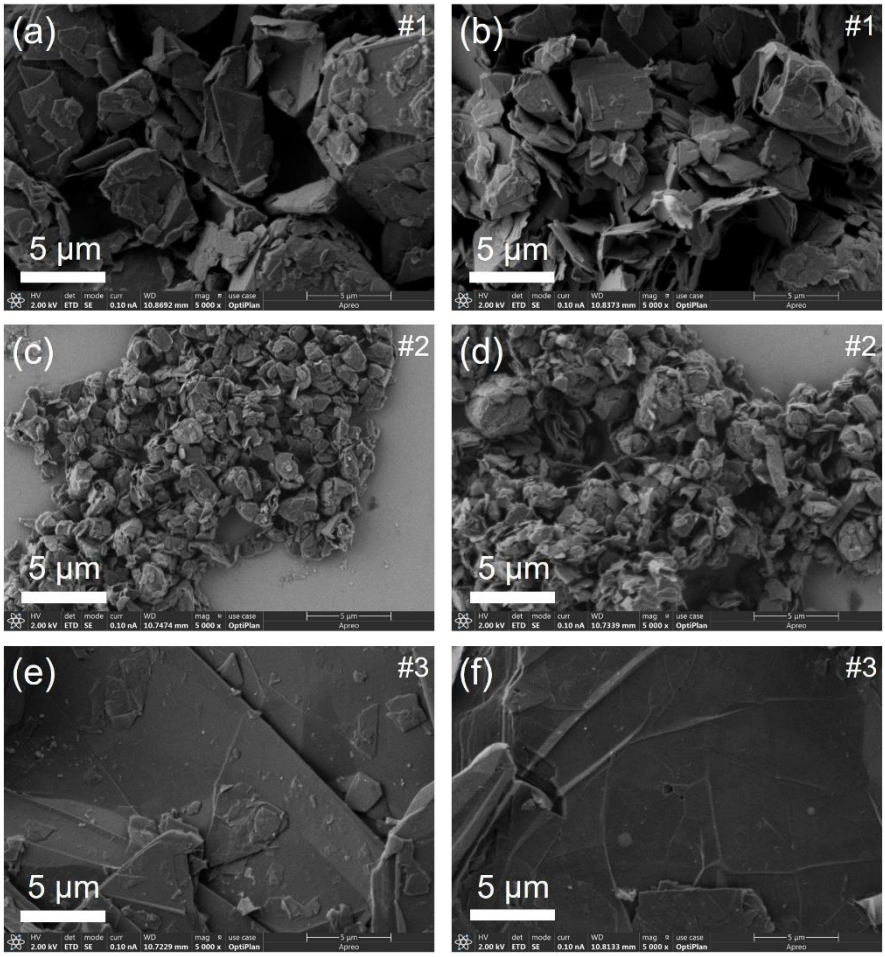

Figure S1. Before annealing (a), (c), (e) and after annealing with α-Li_3N (b), (d), (f).

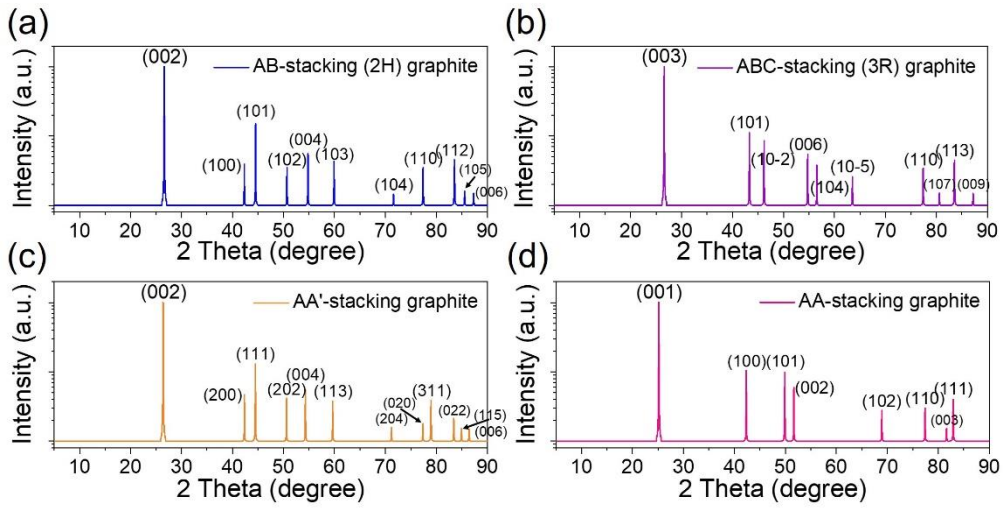

Figure S2. (a) AB-stacking (2H) graphite; (b) ABC-stacking (3R) graphite; (c) AA'-stacking graphite and (d) AA-stacking graphite.

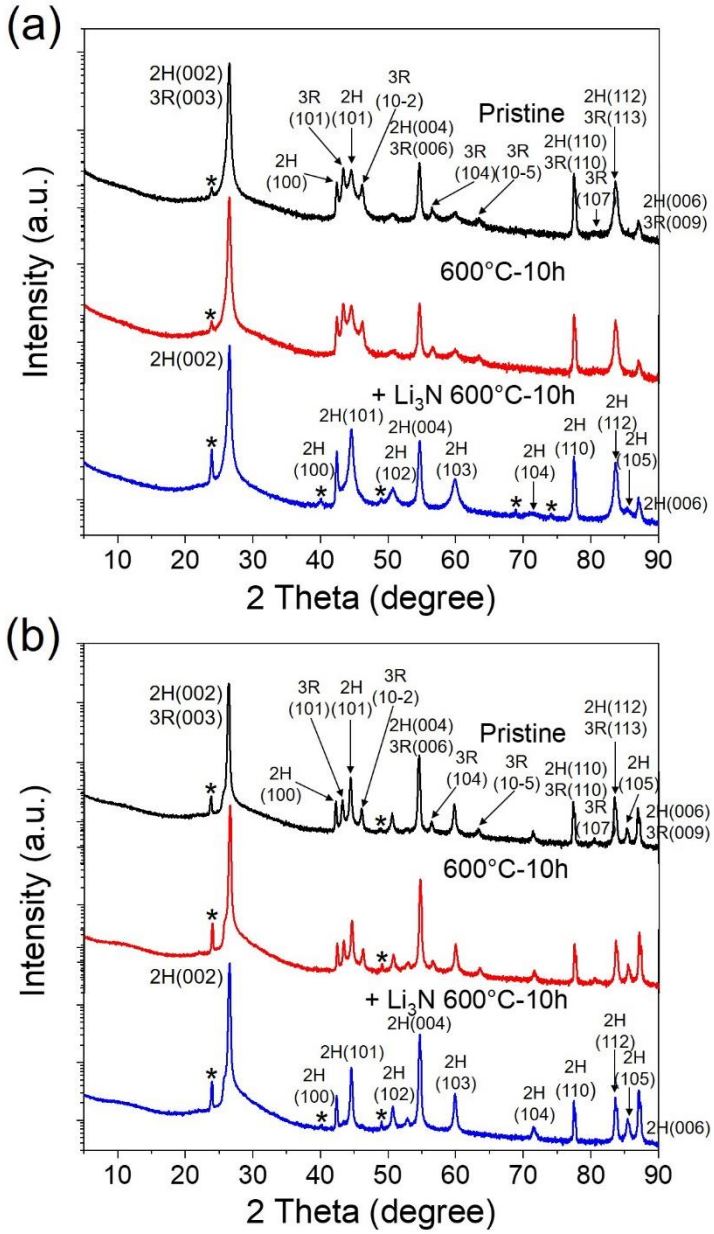

Figure S3. Cu K_α (radiation wavelength λ = 0.15418 nm) powder XRD patterns of (a) #2 graphite and (b) #3 graphite before annealing, after annealing without or with α-Li_3N under 600 °C for 10 h. Peaks corresponding to 2H phase or 3R phase are indicated by the arrows. Asterisks (*) point to the diffraction peaks originated from Cu K_β radiation (radiation wavelength λ = 0.13922 nm).

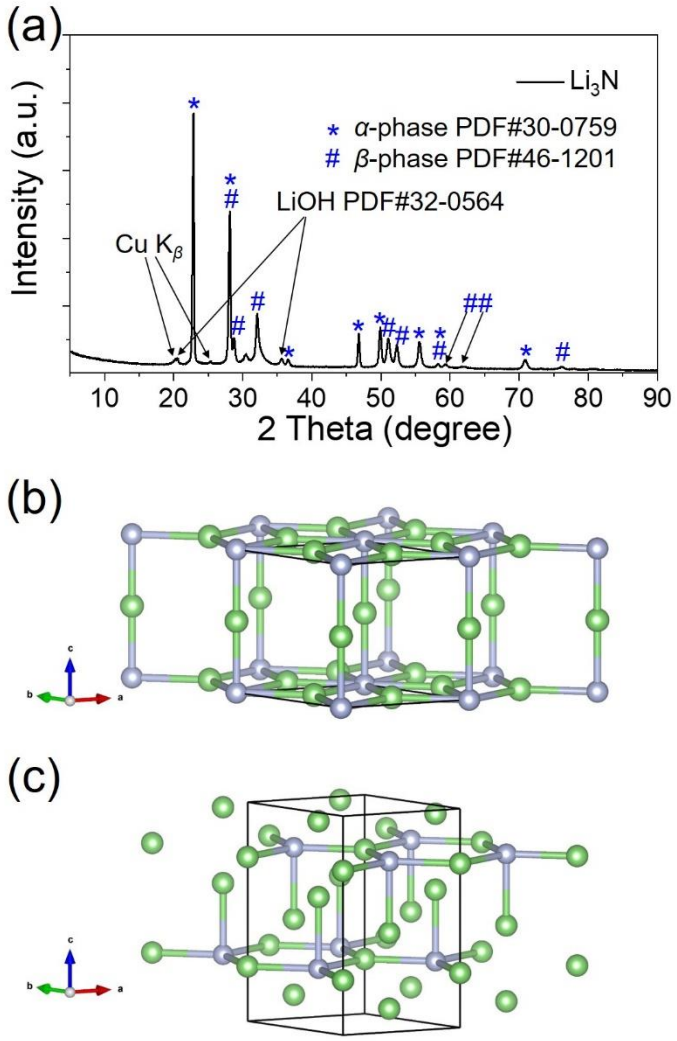

Figure S4. (a) Cu K_α radiation (radiation wavelength λ = 0.15418 nm) powder XRD pattern of Li_3N crystal powder purchased from Sigma-Aldrich. Schematic of atomic structure of (b) α-phase and (c) β-phase Li_3N.

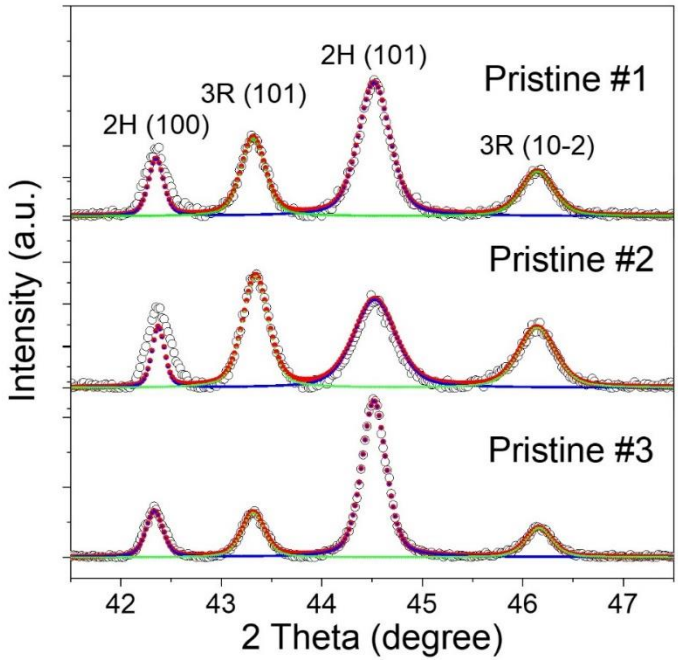

Figure S5. Fitting of Cu K_α (radiation wavelength λ = 0.15418 nm) powder XRD patterns in the fingerprint range from 41.5 ° to 47.5 ° of pristine #1; #2; and #3 graphite sample. ○ Experimental line; ● Fitting line; ■ Fitting line of 2H phase; ▼ Fitting line of 3R phase. Before fitting, background of all XRD patterns were subtracted, and then tiny (all in ± 0.1 °) and integral position shift of abovementioned 4 diffraction peaks were carried out to align the position of experimental and simulated 2H(101) (**Table S2** and **Figure S2**) diffraction peak.

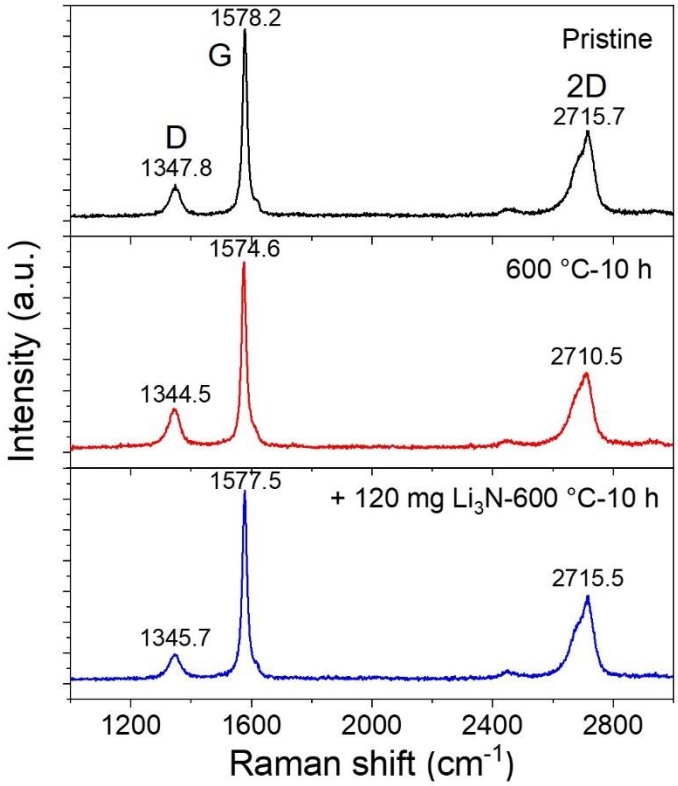

Figure S6. Raman spectra (laser wavelength λ = 532 nm) of #1 graphite sample before annealing (black line), after annealing without (red) or with α-Li_3N (blue).

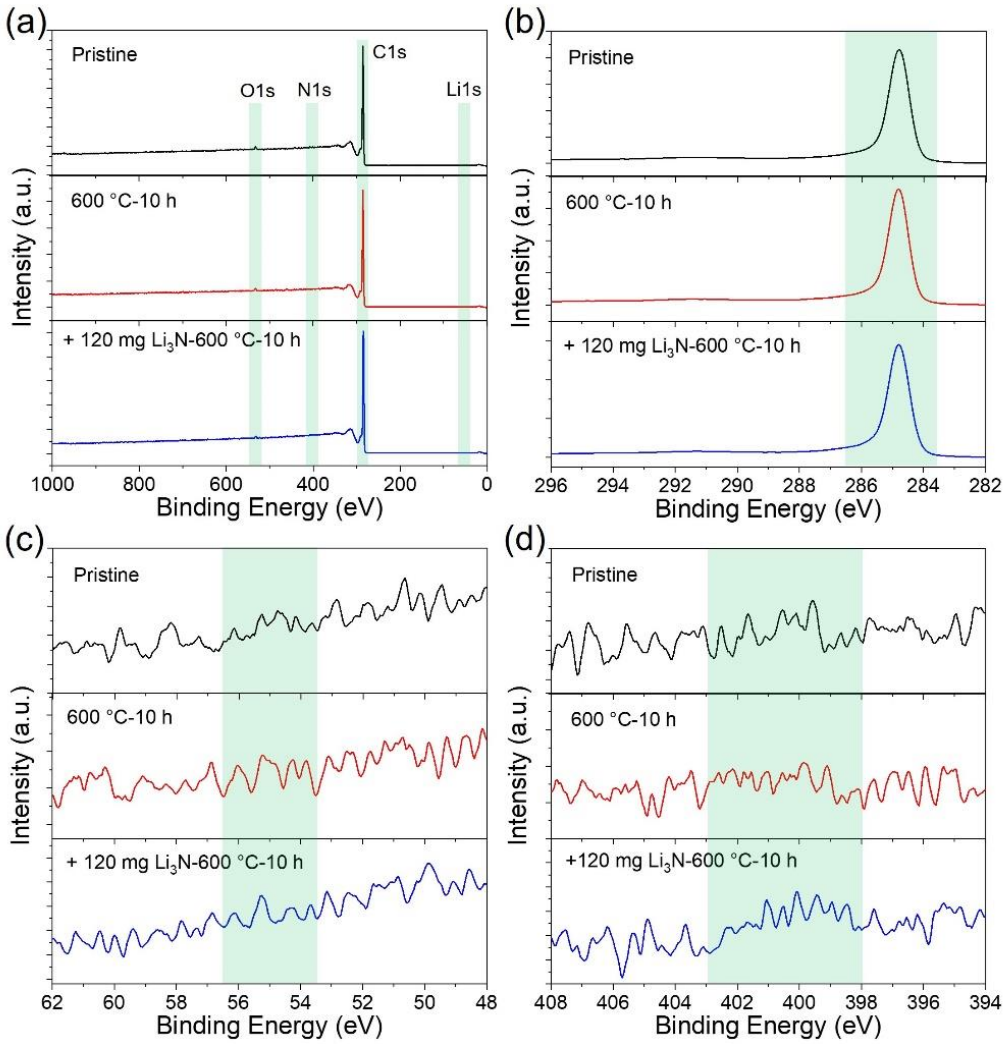

Figure S7. XPS spectra of #1 graphite sample before annealing, after annealing without or with α-Li_3N: (a) Survey; (b) C 1s; (c) Li 1s; (d) N 1s. The shade areas indicate where the peaks are supposed to be.

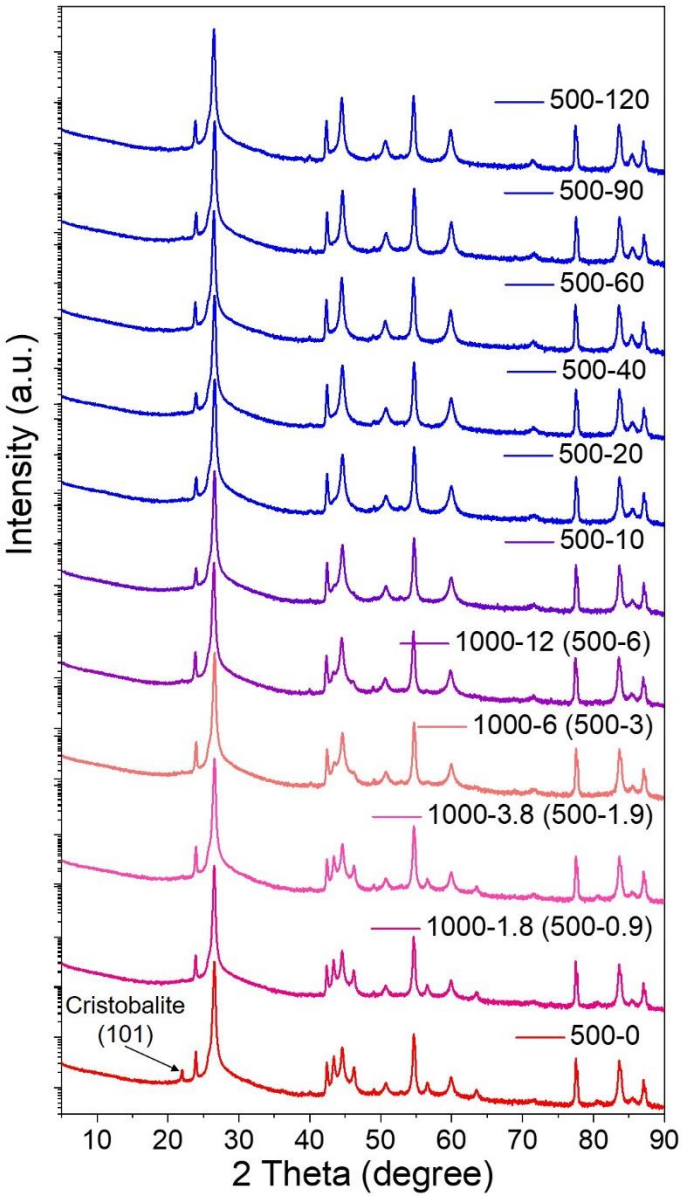

Figure S8. Cu K_α (radiation wavelength λ = 0.15418 nm) powder XRD patterns of 500 mg #1 graphite samples after annealing with 120, 90, 60, 40, 20, 10, 6, 3, 1.9, 0.9, and 0 mg α-Li_3N under 600 °C for 10 h.

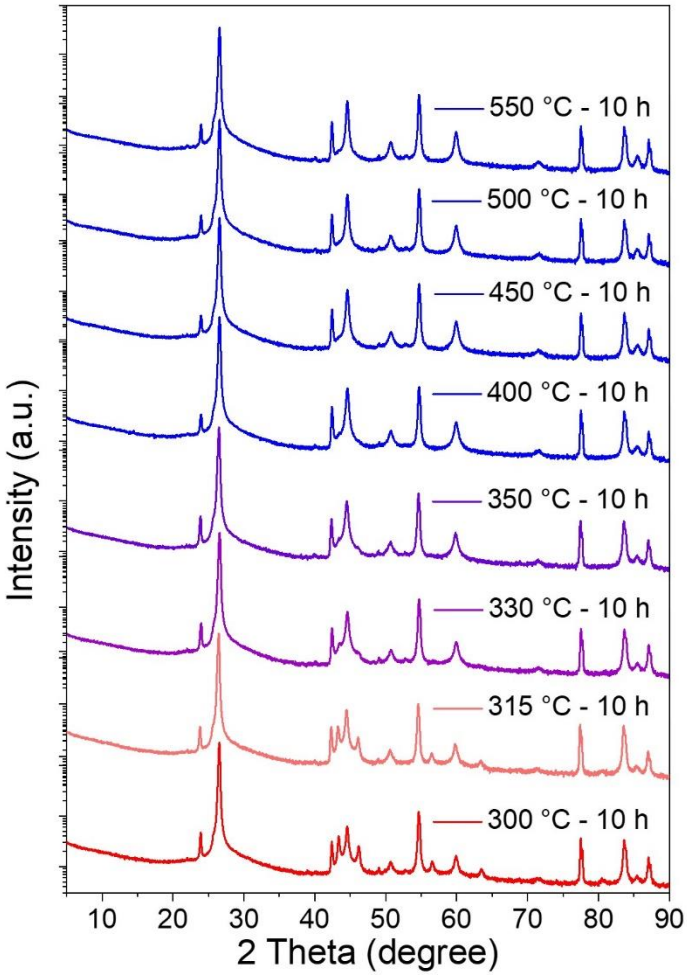

Figure S9. Cu K_α (radiation wavelength λ = 0.15418 nm) powder XRD patterns of 500 mg #1 graphite samples after annealing with 120 mg α-Li_3N under 550 °C, 500 °C, 450 °C, 400 °C, 350 °C, 330 °C, 315 °C and 300 °C for 10 h.

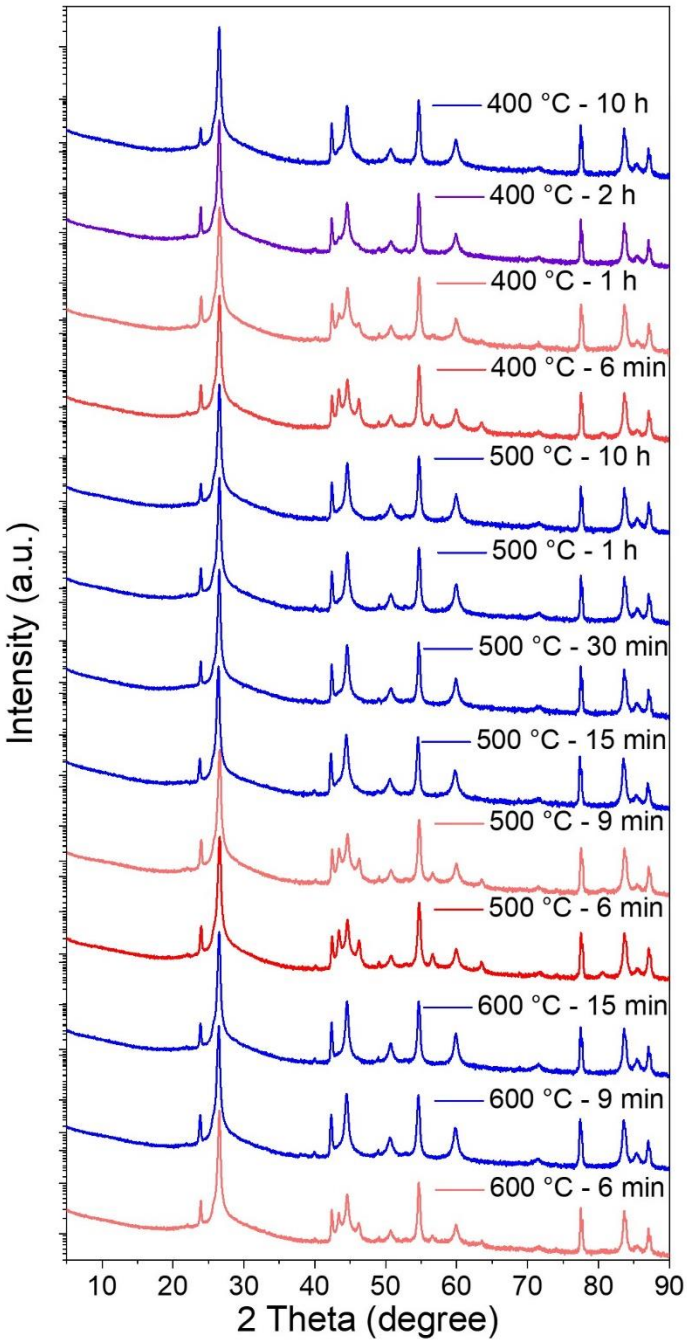

Figure S10. Cu K_α (radiation wavelength λ = 0.15418 nm) powder XRD patterns of 500 mg #1 graphite samples after annealing with 60 mg α-Li_3N under 400 °C for 10 h, 2 h, 60 min and 6 min; under 500 °C for 10 h, 60 min, 30 min, 15 min, 9 min and 6 min; under 600 °C for 15 min, 9min and 6 min (10 h, not including heating time; 2 h ~ 6 min, including time of rapid heating).

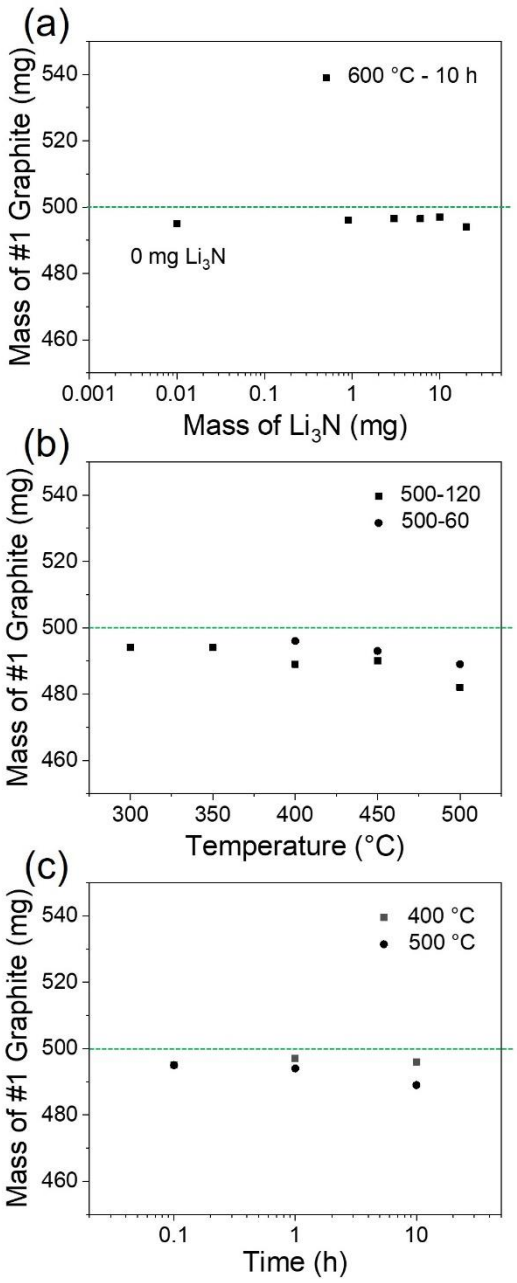

Figure S11. (a) Residual mass of 500 mg #1 graphite sample after annealing with α-Li_3N under different mass ratios at 600 °C for 10 h; (b) Residual mass of 500 mg #1 graphite sample and simulated 3R phase content after annealing with 120 mg α-Li_3N at decreasing temperature from 500 °C to 300 °C for 10 h and 60 mg α-Li_3N at decreasing temperature from 500 °C to 400 °C for 10 h; (c) Residual mass of 500 mg #1 graphite sample after annealing with 60 mg α-Li_3N at 400 °C and 500 °C for 6 min (0.1 h, including time of rapid heating), 60 min (1h, including time of rapid heating), and 600 min (10 h, not including heating time), respectively.

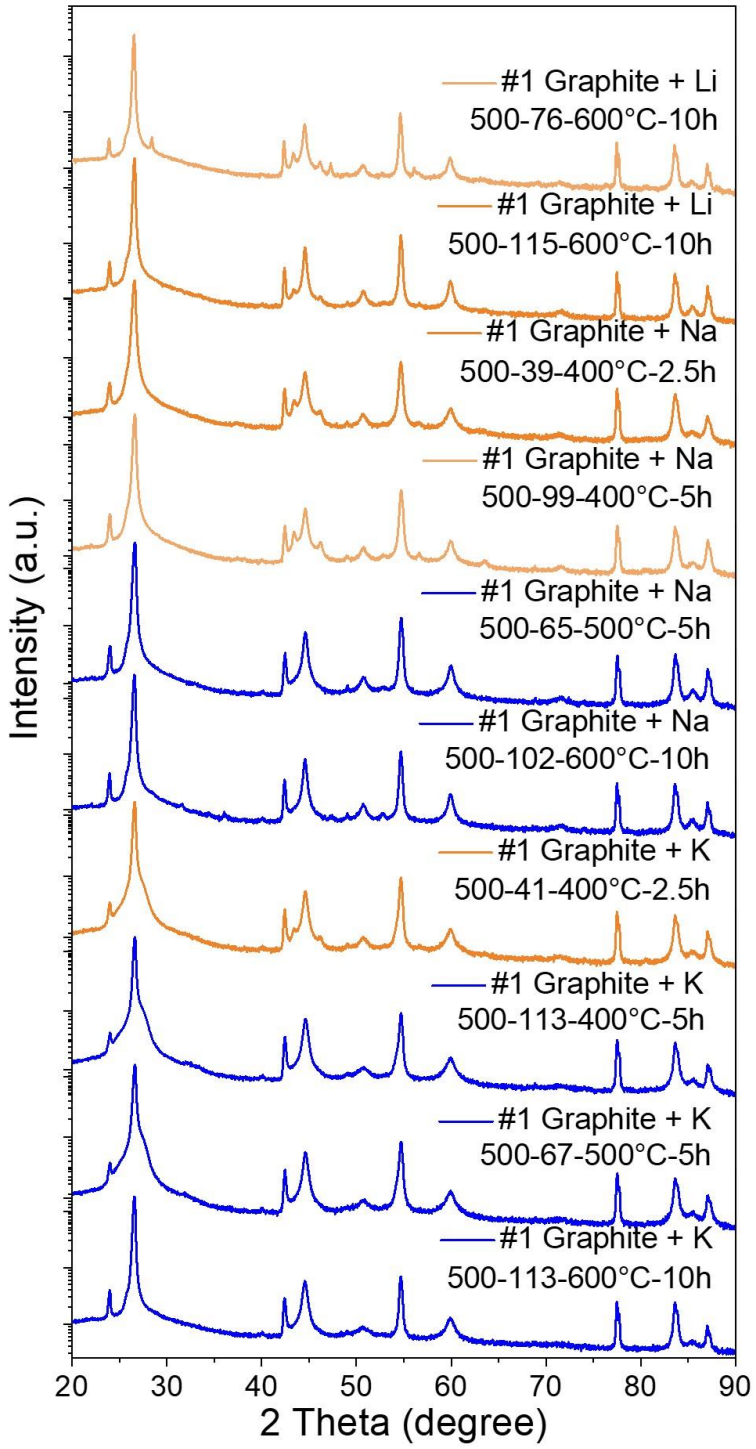

Figure S12. Cu K_α (radiation wavelength $\lambda = 0.15418$ nm) powder XRD patterns of 500 mg #1 graphite samples after annealing with alkali metals Li, Na and K under temperatures from 400 °C to 600 °C. One shall note that Na would not intercalate into #1 graphite under 400 °C ~ 600 °C but K would intercalate into #1 graphite under 400 °C ~ 500 °C.

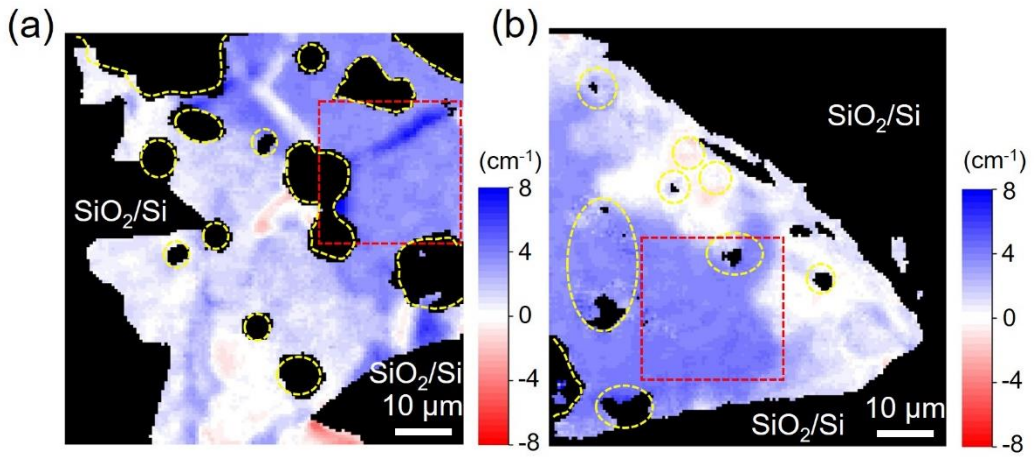

Figure S13. (a) G band position difference mapping, obtained by subtracting the G band positions of pristine graphite from those after α-Li_3N deposition, of the region containing AB-stacking and ABC-stacking graphite; (b) G band position difference mapping of the region containing mainly AB-stacking graphite.

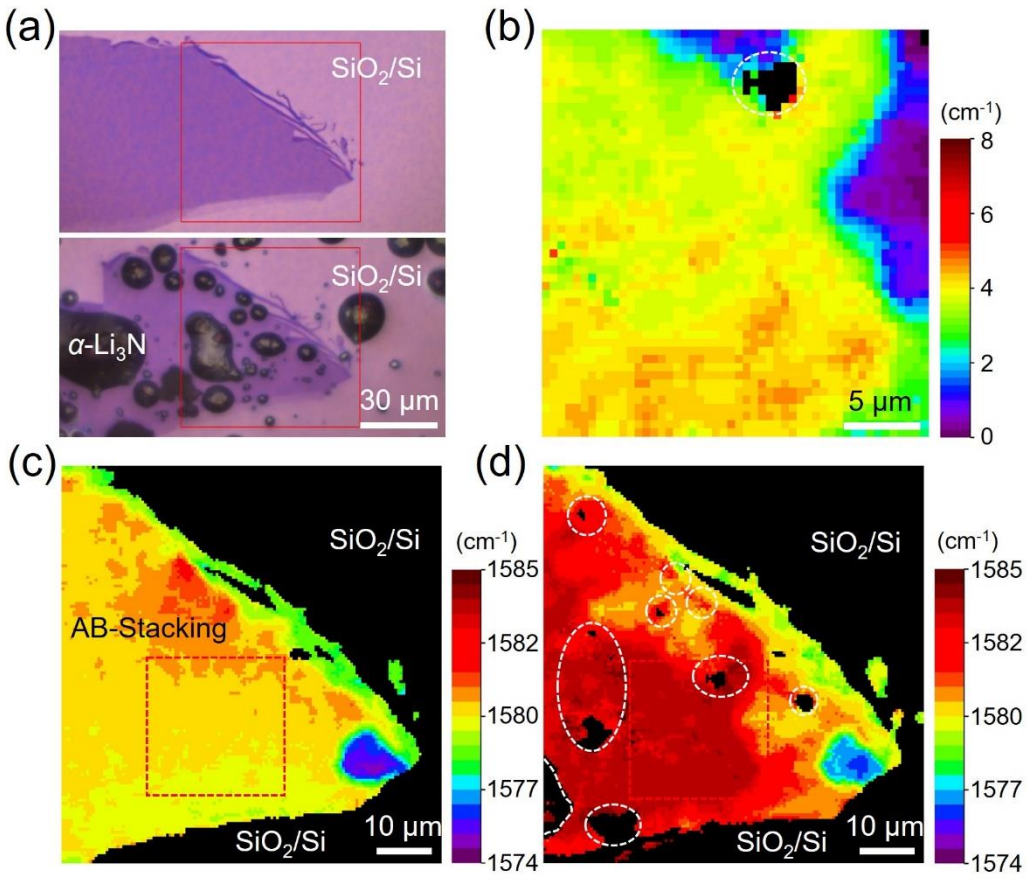

Figure S14. (a) Optical images of AB-stacking region on a mechanically exfoliated graphite flake on a SiO_2/Si substrate before (upper) and after (lower) partial coverage of α-Li_3N particles under room temperature. (b) Difference mapping of Raman G band position excited by a 532 nm laser for the area (AB-stacking) marked by red dashed square in (c) and (d); Raman G band position for the graphite flake on a SiO_2/Si substrate before (c) and (d) after partial coverage of α-Li_3N particles under room temperature. The location of most α-Li_3N particles in (b) and (d) were marked by white dashed lines.

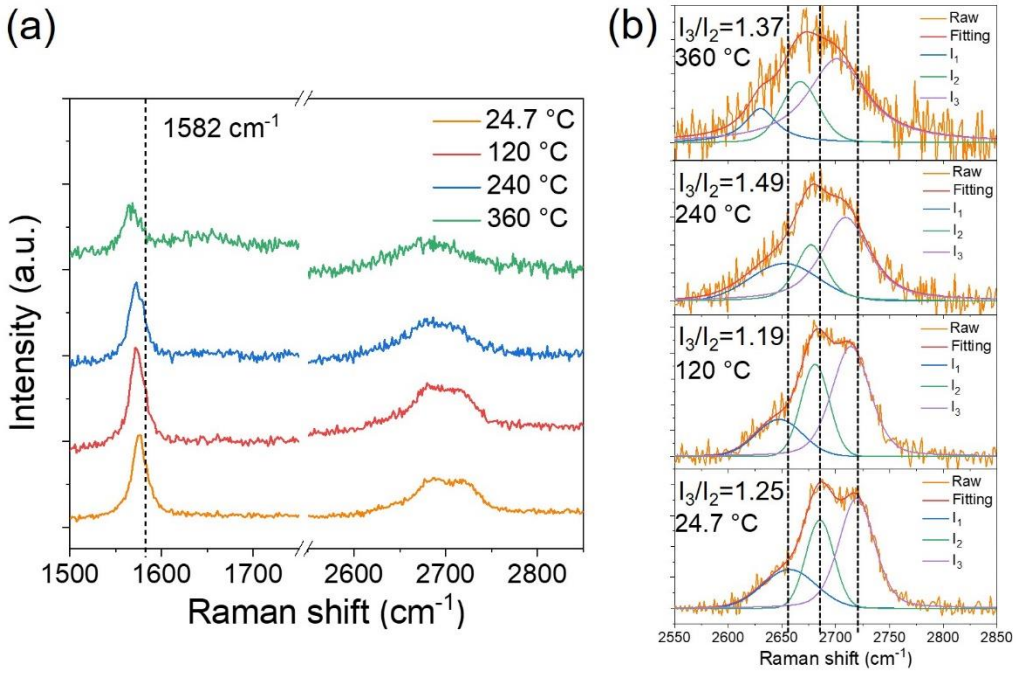

Figure S15. (a) Evolution of 532 nm laser excited Raman G, 2D band intensity, width, and position of a mechanical exfoliated ABC-stacking graphite flake under increasing temperature. (b) Fitting of corresponding 2D band in (a). The 2D band were fitted with mixed Gaussian and Lorentzian peaks.

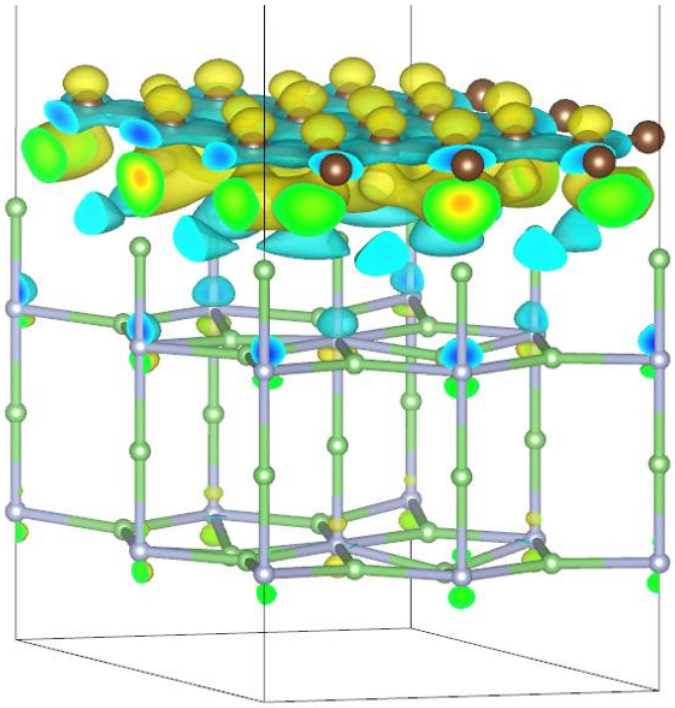

Figure S16. Model used for bader charge analysis and calculated charge deformation density between graphene and Li face of α-Li_3N. The iso-surface value is 0.0013 e^- $bohr^{-1}$.

Table S1. Details of three graphite samples in the experiment.

Name	Graininess	Carbon Purity	Corporation
#1	8000 mesh	99.95%, metals basis	Aladdin Industrial Corporation (Shanghai, China)
#2	D50 < 600 nm	99.95%, metals basis	Aladdin Industrial Corporation (Shanghai, China)
#3	≤ 30 μm (≥ 95%)	≥ 99.85%	Sinopharm Chemical Reagent Co., Ltd (Shanghai, China)

Table S2. Two theta of crystal planes of #1 graphite sample in experiment (Cu K_α XRD, radiation wavelength λ = 0.15418 nm) and simulation (radiation wavelength λ = 0.15418 nm). Among them, five feature diffraction peaks originated from crystal planes of (101), (10-2), (104), (10-5), (107) in 3R phase (red line) would not be covered up by 2H phase and have been used to distinguish the crystal structure effectively.

Crystal planes of 2H phase in #1	(002)	(100)	(101)	(102)	(004)	(103)	(104)	(110)	(112)	(105)	(006)
2 Theta in Experiment	26.45 °	42.32 °	44.48 °	50.63 °	54.59 °	59.83 °	71.36 °	77.42 °	83.55 °	85.44 °	86.96 °
2 Theta in Simulation	26.61 °	42.32 °	44.52 °	50.69 °	54.80 °	59.92 °	71.58 °	77.39 °	83.54 °	85.54 °	87.30 °
Crystal planes of 3R phase in #1	(003)	(101)	(10-2)	(006)	(104)	(10-5)	\	(110)	(107)	(113)	(009)
2 Theta in Experiment	26.45 °	43.28 °	46.11 °	54.59 °	56.48 °	63.45 °	\	77.42 °	80.47 °	83.55 °	86.96 °
2 Theta in Simulation	26.58 °	43.31 °	46.17 °	54.74 °	56.52 °	63.52 °	\	77.39 °	80.56 °	83.53 °	87.20 °

Table S3. XPS atomic ratio in #1 graphite sample before annealing, after annealing without and with α-Li_3N under 600 °C for 10 h.

#1 graphite sample	C1s	O1s	N1s	L1s
Pristine	98.89%	1.11%	0	0
600 °C -10 h	98.95%	1.05%	0	0
+ 120 mg α-Li_3N-600 °C -10 h	98.88%	0.95%	0.18%	0

Table S4. Calculated 3R content of 500 mg or 1000 mg #1 graphite after annealing with α-Li_3N.

Mass of #1 graphite (mg)	Mass of α-Li_3N (mg)	Time (min)	Temperature (°C)	3R content (%)
\	0	\	25	37.657
500	0	600	600	35.890
1000	1.8	600	600	35.357
1000	3.8	600	600	31.344
1000	6	600	600	5.952
1000	12	600	600	3.881
500	10	600	600	0
500	20	600	600	0
500	40	600	600	0
500	60	600	600	0
500	90	600	600	0
500	120	600	600	0
500	120	600	550	0
500	120	600	500	0
500	120	600	450	0
500	120	600	400	0
500	120	600	350	0.688
500	120	600	330	3.225
500	120	600	315	25.804
500	120	600	300	35.575
500	60	600	550	0
500	60	600	500	0
500	60	600	450	0
500	60	600	400	0
500	60	6	600	20.822
500	60	9	600	0
500	60	15	600	0

500	60	6	500	35.760
500	60	9	500	27.536
500	60	15	500	0
500	60	30	500	0.842
500	60	60	500	0
500	60	6	400	35.929
500	60	60	400	10.221
500	60	120	400	4.331
\	0	120	2750	4.987

Table S5. Calculation method test for PBE-BJD3 method, SCAN-rvv10 method and optB88 method.

PBE-BJD3	0.06 e^-	neutral	0.06 h^+
2H Total energy (eV)	-37.17848298	-37.46738228	-37.737228
AA Total energy (eV)	-37.17480236	-37.43259724	-37.6768085
AA' Total energy (eV)	-37.17598132	-37.46178864	-37.7284387
E(AA)-E(2H) (meV/atom)	0.920155	8.69626	15.10487
E(AA')-E(2H) (meV/atom)	0.625415	1.39841	2.1973175
SCAN-rvv10	0.06 e^-	neutral	0.06 h^+
2H Total energy (eV)	-39.85750269	-40.16253682	-40.4388693
AA Total energy (eV)	-39.84589599	-40.11761276	-40.3693746
AA' Total energy (eV)	-39.852357	-40.15359857	-40.4283749
E(AA)-E(2H) (meV/atom)	2.901675	11.231015	17.37366
E(AA')-E(2H) (meV/atom)	1.2864225	2.2345625	2.6236025
optB88	0.06 e^-	neutral	0.06 h^+
2H Total energy (eV)	-31.82853103	-32.11730536	-32.3819331
AA Total energy (eV)	-31.81762008	-32.07581039	-32.3178378
AA' Total energy (eV)	-31.82400811	-32.11080482	-32.3728227
E(AA)-E(2H) (meV/atom)	2.7277375	10.3737425	16.02381
E(AA')-E(2H) (meV/atom)	1.13073	1.625135	2.2775875

REFERENCES

(1) Hafner J. Ab‐initio simulations of materials using VASP: Density‐functional theory and beyond. *J. Comput. Chem.* **2008**, *29*, 2044-2078.

(2) Perdew J. P.; Burke K.; Ernzerhof M. Generalized gradient approximation made simple. *Phys. Rev. Lett.* **1996**, *77*, 3865-3868.

(3) Klimes J.; Bowler D. R.; Michaelides A. Chemical accuracy for the van der Waals density functional. *J. Phys.: Condens. Matter* **2010**, *22*, 022201.

(4) Ernzerhof M.; Scuseria G. E. Assessment of the Perdew–Burke–Ernzerhof exchange-correlation functional. *J. Chem. Phys.* **1999**, *110*, 5029-5036.

(5) S. Grimme, S. Ehrlich, L. Goerigk, Effect of the damping function in dispersion corrected density functional theory. *J. Comput. Chem.* **2011**, *32*, 1456-1465.

(6) H. Peng, Z. Yang, J. P. Perdew, J. Sun, Versatile van der Waals density functional based on a meta-generalized gradient approximation. *Phys. Rev. X* **2016**, *6*, 041005.

(7) Pan, F.; Wang, Y. H.; Chen, C. “Basic Property of X-ray” in *X-ray Diffraction Technology* (Chemical Industry Press, Beijing) **2016**, pp. 15-17.

(8) David W. I. F. Powder diffraction peak shapes. Parameterization of the pseudo-Voigt as a Voigt function. *J. Appl. Crystallogr.* **1986**, *19*, 63-64.